



CHORUS

This is the accepted manuscript made available via CHORUS. The article has been published as:

L-shell x-ray emission from neonlike W^{64+}

P. Beiersdorfer, J. K. Lepson, M. B. Schneider, and M. P. Bode

Phys. Rev. A **86**, 012509 — Published 18 July 2012

DOI: [10.1103/PhysRevA.86.012509](https://doi.org/10.1103/PhysRevA.86.012509)

L-shell X-ray Emission from neonlike W⁶⁴⁺

P. Beiersdorfer^{1,2}, J. K. Lepson^{2,3}, M. B. Schneider¹, M. P. Bode³

¹*Physics Division, Lawrence Livermore National Laboratory, Livermore, CA 94550, USA*

²*Department of Chemistry and the Chemical Physics Program,*

University of Puerto Rico, San Juan, PR 00931, USA and

³*Space Sciences Laboratory, University of California, Berkeley, CA 94720, USA*

Abstract

We present high-resolution crystal spectroscopy measurements of the $n = 3 \rightarrow n = 2$ L-shell x-ray transitions of neonlike W⁶⁴⁺, which include seven electric dipole allowed transitions, two electric quadrupole transitions, and one magnetic quadrupole transition. The resulting wavelength data are compared to recent calculational results, allowing us to clearly distinguish between different theoretical approaches, which need to take into account not only substantial electron correlations effects but also radiative contributions, which in case of the transition from upper level $(1s^2 2s_{1/2} 2p^6 3p_{3/2})_{J=1}$ to the closed-shell neonlike ground state exceeds 20 eV. Best agreement is found with calculations utilizing the relativistic multi-reference Møller-Plesset approach. In addition to the emission from W⁶⁴⁺, we have observed several innershell collisional satellite lines associated with oxygenlike W⁶⁶⁺, fluorinelike W⁶⁵⁺, sodiumlike W⁶³⁺, and magnesiumlike W⁶²⁺, which provide benchmarks for future calculations as well as for recent calculations using the relativistic many-body perturbation theory. The present measurements also provide accurate rest wavelengths for establishing the instrumental dispersion needed for future measurements of the core plasma motion in the ITER tokamak and show that the candidate W⁶⁴⁺ line for such measurements remains well isolated from neighboring collisional satellite lines even when broadened by the expected, high temperatures in this device.

PACS numbers: 32.30.Rj, 34.80.Dp, 52.25.Vy, 52.70.La

I. INTRODUCTION

The ground configuration of neonlike ions, $(1s^2 2s^2 2p^6)_{J=0}$, consists of completely filled K and L shells. As a result, radiative transitions between excited states and ground must change the principal quantum number n by $\Delta n \geq 1$ and thus are typically in the x-ray regime for all ions except those with the lowest atomic number Z .

As is the case with heliumlike ions, which have a completely filled K-shell as their ground configuration, neonlike ions produce very bright x-ray emission and are readily observed in high-temperature plasma. As a result, x-ray spectra from neonlike ions have been developed for plasma diagnostics. For example, the soft x-ray emission from neonlike iron is a dominant component of many astrophysical spectra, including those formed by stellar coronae [1–3] and galaxies [4–6]. Neonlike ions from higher- Z ions, such as selenium ($Z = 34$), have been used to determine transport and ion confinement times in tokamak plasma [7, 8], while neonlike ions of molybdenum ($Z = 42$) have been used to determine plasma rotation [9] and neonlike molybdenum, neonlike silver ($Z = 47$), and neonlike xenon ($Z = 54$) ions have been used to determine electron temperature and density in laser-produced plasmas [10, 11]. Neonlike ions have also played a crucial role in developing soft x-ray lasers [12], where neonlike ions as high as silver were made to lase [13].

The spectroscopic study of tungsten has become of great interest because of tungsten's renewed role in magnetic fusion and radiation source development [14–16]. Recent measurements have included those of near-lithiumlike tungsten (W^{71+}) [17], near-sodiumlike tungsten (W^{61+}) [18, 19], near-nickellike tungsten (W^{46+}) [20–24], near-palladiumlike tungsten (W^{28+}) [25], promethiumlike tungsten (W^{15+}) [26], and near-ytterbiumlike tungsten (W^{4+}) [27]. The spectrum of neonlike tungsten has become of particular interest as a working medium for the proposed crystal spectrometer for the ITER (Latin "the way") tokamak under construction in France [28]. The ITER tokamak is predicted to achieve core electron temperatures in excess of 20 keV. At this temperature, the ions of the constituent metals of

stainless steel would have burned out, and higher- Z elements would have to be introduced for diagnostic purposes. Indeed, it was proposed to introduce Kr for this purpose, and a spectrometer based on the observation of heliumlike Kr^{34+} was proposed [29]. However, tungsten will be an indigenous impurity in ITER because of various first-wall components that have to bear the high heat load while not retaining tritium. Hence, tungsten will be a component of ITER plasmas and, unlike krypton, does not need to be added. Moreover, neonlike W^{64+} reaches its maximum abundance in the core of ITER fusion plasmas [28]. As a result, it was thought that the strongest line of the W^{64+} spectrum provided an excellent means for measuring the plasma ion temperature and bulk ion velocity based on its broadening and shift [28, 30]. Accurate knowledge of the rest energy of the line is thus of great importance for such diagnostic applications as bulk plasma velocity measurements. A high-resolution spectrum of neonlike tungsten has been reported before by Biedermann et al., who observed it at the Berlin electron beam ion trap [31]. However, no wavelength values were reported.

The energy levels of neonlike ions are also of great interest to atomic physics, as they represent a stepping stone toward developing accurate methods for generating energy levels of multi-electron ions. Early high-resolution measurements of the x-ray transitions of neonlike ions ranging from silver to europium ($Z = 63$) revealed systematic offsets of up to several eV between measured energies and those calculated with the multi-configuration Dirac-Fock method [32–34]. Improvements in the calculated energies were achieved by adding corrections due to ground-state correlations and by noting the importance of so-called Coster-Kronig and super Coster-Kronig fluctuations [32, 33, 35, 36]. Additionally, the importance of quantum electrodynamics (QED) in calculating the transition energies was noted.

Accurate measurements of neonlike transitions beyond those of Eu^{53+} carried out on the Princeton Large Torus tokamak [33] are needed to further guide theory. Measurements using the beam-foil technique have provided data on neonlike gold and neonlike bismuth [35, 36], although with greatly reduced accuracy compared to the tokamak data. Measurements using

electron beam ion traps have produced high- Z data for neonlike ytterbium ($Z = 70$) and neonlike thorium and uranium ($Z = 90, 92$) [37, 38]. In these cases, only partial spectral data were reported. For example, the ytterbium measurement focused on the shortest-wavelength neonlike $n = 3 \rightarrow n = 2$ transitions in order to determine contributions from QED, and a value of 18.4 ± 0.8 eV was found for the self-energy contribution to the $3p_{3/2} \rightarrow 2s_{1/2}$ transition energy [37]. The few existing measurements of high- Z neonlike ions beyond Eu^{53+} are not yet sufficient to determine the iso-electronic trend of neonlike spectra with the high accuracy needed to test modern theoretical approaches toward calculating multi-electron atomic structure.

In the following we report high-resolution measurements of the x-ray spectrum of neonlike tungsten carried out at an electron beam ion trap. Our measurements include all seven electric-dipole allowed $n = 3 \rightarrow n = 2$ transitions as well as three dipole forbidden transitions. The accuracy of our measurements is comparable to that achieved in the earlier tokamak measurements of Ag^{37+} through Eu^{53+} , and exceeds that achieved in the high- Z beam-foil measurements by factors of three to ten. Our measurements, thus, provide an important step along the neonlike iso-electronic sequence for testing theory. In particular, calculations of neonlike tungsten have recently been reported that use the relativistic multi-reference Møller-Plesset approach [39]. Calculations using this approach have been found to be of very high accuracy when compared to experiment. But so far comparisons with experiment have been limited to transition energies in the extreme ultraviolet or soft x-ray regime below 1 keV [40, 41]. Our measurements, thus, provide the first assessment of this method for x-ray transitions of high- Z ions. We, furthermore, report on several collisional satellite lines, which provide benchmarks for future multi-electron calculations. In this case, there is one calculation available, which was carried out for sodiumlike tungsten based on relativistic many-body perturbation theory [42]. We are also able to assess its accuracy.

II. CALCULATIONS

Because of their fundamental interest to atomic theory, varied calculational techniques have been employed to calculate the energy levels of neonlike ions. These approaches include the parametric potential method [43, 44], the MCDF method [45], and many-body perturbation theory (MBPT) [46, 47]; the latter has recently been extended to include third order Breit terms [48]. Despite the many approaches, unfortunately, only few publications have reported systematic calculations on ions, such as neonlike tungsten, that had not yet been measured at the time of the calculation. Consequently, there are very few calculations for neonlike W^{64+} in the literature.

In Table I, we list the transition energies predicted by the calculations of Ivanova and Gulov [49], who used the relativistic perturbation theory with model potential approach, and of Vilkas et al. [39], who used the relativistic multi-reference Møller-Plesset approach to second order. Inspection of Table I shows that the values obtained by the two approaches differ substantially.

In addition to previously published results, we have performed our own calculations using the Flexible Atomic Code (FAC) developed by Gu [50]. It employs the configuration interaction (CI) approach to determine the atomic structure. Because structure calculations involving only the ground state and all 36 excited levels with a $2s$ or $2p$ vacancy and a valence electron in the $3s$, $3p$, or $3d$ configuration have been sufficient to produce accurate results before for neonlike iron ($Z = 26$) [51], we have performed such calculations also for neonlike tungsten. The results are included in Table I. We have, furthermore, carried out FAC calculations for the neighboring charge states of neonlike tungsten. These structure calculations also involve only the ground state and all excited levels with a $2s$ or $2p$ vacancy and valence electrons in the $3s$, $3p$, or $3d$ configuration.

FAC, moreover, allows us to construct detailed collisional radiative models, which were used to identify the various L-shell tungsten lines in our measured spectra. We have made

calculations to predict the spectral lines of W^{64+} in the wavelength range of interest, as shown in Fig. 1. We have also made calculations of the line emission from the neighboring ion states. In particular, we have calculated the spectral emission from the autoionizing sodiumlike W^{63+} , magnesiumlike W^{62+} , and aluminumlike W^{61+} ions. The results of these calculations are shown in Fig. 2. Because the electrons in our measurements are mono-energetic with a small spread of about 50 eV [38, 52], no dielectronic recombination resonances are excited and the lines shown in Fig. 2 comprise only collisional satellites. We have also calculated the spectral emission from fluorinelike W^{65+} and oxygenlike W^{66+} . The results are shown in Fig. 3.

FAC has been used extensively to produce L-shell emission spectra for line identification. For example, FAC was recently used to model and identify the L-shell spectral features of neonlike through lithiumlike aluminum ($Z = 13$) [53], iron ($Z = 26$) [54], and nickel ($Z = 28$) [55]. Following the approaches used in these calculations, our calculations included all energy levels, radiative transition rates, and collisional excitation cross sections connecting the ground level and all excited levels with a $2s$ or $2p$ vacancy and a valence electron in the $3s$, $3p$, or $3d$ configuration with each other. The parameters of these collisional radiative models closely follow the experimental condition in the electron beam ion trap, as discussed in the next section, i.e., an electron beam energy of 15 – 21 keV and an electron density of $5 - 10 \times 10^{11} \text{ cm}^{-3}$. The model for each tungsten ion assures that density-sensitive effects are accounted for, although such effects are essentially absent at the (low) densities found in our spectroscopic source.

III. EXPERIMENT

The measurements were performed on the EBIT-I electron beam ion trap at the Lawrence Livermore National Laboratory, which is the first such machine of its kind [56, 57]. Tungsten ions were produced and excited by the EBIT-I electron beam at energies between 15 and 21

keV and currents of about 150 mA. The tungsten spectra were calibrated by observing the K-shell emission lines of helium- and hydrogenlike titanium, vanadium, copper, and zinc. An overview of the location of the tungsten lines relative to those of the calibration lines is shown in Fig. 1.

The spectra were recorded with a von Hámos-type crystal spectrometer. This spectrometer is well matched to the narrow line source formed by the electron beam and provides high photon throughput with moderately high spectral resolution. The instrument has been used on EBIT-I to measure a variety of x-ray spectra [58–62]. A detailed description of the basic properties of the spectrometer is given in Ref. [63].

For the present measurements the spectrometer was modified to access the wavelength region between 1.10 and 1.55 Å. For this purpose, the spectrometer uses a 12 cm × 5 cm × 0.02 cm LiF(200) crystal, which has been bent cylindrically to a radius of curvature of 30 cm. The $2d_\infty$ spacing of this crystal plane is equal to 4.027 Å [64]. A multiwire proportional counter similar to the one described by Vogel et al. [65] with a sensitive area of 10 × 3 cm² was employed to record the spectra. The counter was filled with a mixture of 90% xenon and 10% methane. The pulse height signal from the detector allowed us to set a window on the energy of the x rays of interest and thus to reduce the background from cosmic rays and terrestrial radiation. When measuring spectra in second order, we placed an aluminum foil in front of the detector, in order to reduce the number of photons being detected in first order.

The spectrometer allowed us to measure a spectral region of about 0.15 Å. This was insufficient to measure the full range between 1.10 and 1.55 Å needed to observe all seven dipole allowed $n = 3 \rightarrow n = 2$ lines in neonlike tungsten. Instead, four settings were necessary, each of which needed to be calibrated separately. In particular, we observed the region between 1.40 and 1.55 Å, which contained the K-shell lines of heliumlike Cu²⁷⁺ and hydrogenlike Cu²⁸⁺; the region between 1.3 and 1.4 Å, which contained the K-shell lines of heliumlike Zn²⁸⁺ and hydrogenlike Zn²⁹⁺; the region between 1.2 and 1.35 Å, which

was observed in second order and which contained the K-shell lines of heliumlike Ti^{20+} and hydrogenlike Ti^{21+} in first order; and the region between 1.1 and 1.25 Å, which also was observed in second order and which contained the K-shell lines of heliumlike V^{21+} and hydrogenlike V^{22+} in first order. An overview of the location of the calibration spectra is given in Fig. 1.

Sample tungsten spectra, together with the various calibration spectra, measured on EBIT-I are shown in Figs. 4–7. The neonlike lines are labeled using the notation of Parkinson [66], augmented by the notation of Beiersdorfer et al. [33] for labeling the electric-dipole forbidden lines. These labels have also been used in Table I, which gives the specific levels associated with each line. The collisional satellite lines from oxygenlike, fluorinelike, sodiumlike, magnesiumlike, and aluminumlike tungsten are labeled using the notation used in Figs. 2 and 3 to denote the strongest predicted lines. We use the labels w , x , y , and z introduced by Gabriel [67] to denote the heliumlike transitions from levels $1s2p\ ^1P_1$, $1s2p\ ^3P_2$, $1s2p\ ^3P_1$, and $1s2s\ ^3S_1$ to the $1s^2\ ^1S_0$ ground state, respectively. The $2p_{3/2} \rightarrow 1s_{1/2}$ and the $2p_{1/2} \rightarrow 1s_{1/2}$ transitions in the hydrogenlike reference spectra are labeled $\text{Ly-}\alpha_1$ and $\text{Ly-}\alpha_2$, respectively.

Hydrogenlike and heliumlike ions are the simplest atomic systems, and their wavelengths are known from theory to a high degree of accuracy, as tested by numerous measurements [68–71]. As a result, they have been used in a variety of measurements as reference standards. In the present case we have used the wavelengths calculated by Johnson and Soff [72] and by Drake [73] as reference standards.

Reference spectra were taken interleaved with recording the tungsten spectra, i.e., before and after as well as in between recording the tungsten spectra. We noted small drifts in the position of the spectral lines, which we could associate with electronic drifts. In order to compensate for such drifts, we installed a collimated ^{55}Fe radioactive source, which formed a narrow x-ray feature at one location on the detector. The ^{55}Fe feature can be seen in Fig. 5(a). This spectrum was recorded with the ^{55}Fe source placed near the center of the

detector. In all other spectra, the ^{55}Fe source was placed to one side of the detector. Using this feature we could monitor electronic drifts and make adjustments, if there were drifts between the calibration and tungsten spectra.

The measurements performed at the longest wavelength were made with a metal vapor vacuum arc (MeVVA) injector [74] consisting of a tungsten anode and a copper trigger wire. Depending on the polarity of the electrodes, either tungsten or copper is preferentially injected, although small amounts of the other material are also injected. As a result, both elements could be seen in a given spectrum, as illustrated in Fig. 4, although with greatly reduced intensities. For measurements in the adjoining wavelength range, we switched between the W/Cu MeVVA and a Yb/Zn MeVVA so that only one of two elements was observed.

Barium is an indigenous impurity of EBIT-I plasmas [57, 75], but it does not have lines in the wavelength range of the neonlike tungsten lines. However, barium has lines at twice the wavelength of the tungsten lines, and barium lines can be seen in the first order calibration spectra of titanium and vanadium (cf. Fig. 6 and Fig. 7). The barium lines do not appear in the tungsten spectra measured in second order shown in Figs. 6 and 7. This is because of the pulse height discrimination used to screen out unwanted signal and because of the aluminum absorber placed in front of the detector, which also screens out lower-energy x rays, as mentioned above. However, we have used barium as a common reference to both the calibration and the tungsten spectra in order to check for spectral drift. In the course of the first/second order measurement series, we were able to use either a W/Ti or a W/V MeVVA without cross-contamination of either the tungsten or calibration spectra.

The short-wavelength (highest x-ray energy) spectrum shown in Fig. 7 has several unidentified features, one of which has been tentatively attributed to a line in neonlike mercury (Hg^{70+}). The spectral emission of W^{64+} is weak in this region (cf. Fig. 1), and the unknown lines are also weak. Mercury has been noted as a contaminant in EBIT-I before and was likely introduced via the MeVVA injection of gold in prior experiments, as Hg is a (minor) contaminant constituent of gold. Unlike gold, however, mercury has a very high vapor pres-

sure and does not plate out on the vacuum components of EBIT-I. As it accumulates, its spectra add to those of other elements. Subsequent to these measurements, mercury was eliminated from our machine by cleaning of the trap components.

Because some of the tungsten wavelengths were determined by comparing first and second order spectra, care must be taken to account for the fact that crystals have a different index of refraction depending on the order of reflection n . In general, the wavelength $n\lambda$ of a given line is given by Bragg's law [76]

$$n\lambda = 2d_\infty(1 - (2d_\infty)^2\delta/(n^2\lambda^2)) \sin \theta \quad (1)$$

where d_∞ is lattice spacing of the crystal, θ is the Bragg angle, and δ is the deviation of the index of refraction from unity. The value of δ/λ^2 is taken to be independent of wavelength and equal to $3.14 \times 10^{-6} \text{ \AA}^{-2}$ for LiF [76]. Hence, we can use the more familiar form of Bragg's law

$$n\lambda = 2d_n \sin \theta \quad (2)$$

by realizing that in first order reflection $2d_1 = 4.0267949 \text{ \AA}$ and in second order reflection $2d_2 = 4.02694873 \text{ \AA}$.

Finally, we note that the line width is purely instrumental. The temperature of the ions in EBIT-I has been measured both for heliumlike and neonlike ions [77–80] to be a few hundred eV for typical operation conditions of the EBIT-I device. The line widths associated with such temperatures are much smaller than the resolution of the spectrometer. Similarly, there is no line broadening or shift due to blending with dielectronic satellite lines. Unlike in a plasma or beam-foil source, such lines are not excited at the energies of the electron beam in our measurements.

IV. LINE IDENTIFICATION

We have identified ten lines in neonlike W^{64+} . In addition, we have observed several collisional satellite lines in sodiumlike W^{63+} and magnesiumlike W^{62+} . By raising the electron

beam energy above the ionization threshold of W^{64+} , we have produced fluorinelike W^{65+} and oxygenlike W^{66+} . We have firmly identified and measured the wavelength of five fluorinelike features that we attribute to eight transitions. We have also identified several lines in the oxygenlike tungsten spectrum. The line identifications and observed wavelengths are listed in Tables I through V. Details for each charge state are given below.

A. W LXV spectral lines

The strongest neonlike lines – the electric dipole lines $3G$ and $3D$ and the magnetic quadrupole line $M2$ – are readily identified in Figs. 4 and 5. These lines are also very strong in neonlike ions with lower atomic number Z . The other electric dipole allowed lines that are strong in lower- Z neonlike ions, i.e., line $3C$, which is the strongest line from Fe^{16+} ions, and line $3F$ are weak in W^{64+} . Nevertheless, these lines are the strongest in their respective spectra shown in Figs. 6 and 7. The upper levels of these lines have changed their relative energy order established at low atomic number by LS-coupling and are assuming their high- Z ordering given by JJ-coupling [48, 51, 81]. This is why the alphabetical ordering of lines $3A$ through $3G$ no longer follows the energy order established in iron and observed by Parkinson [66]. The remaining electric-dipole allowed neonlike lines, i.e. lines $3A$, $3B$, and $3E$ seen in Fig. 5 and 7, are weak compared to lines $3D$, $3G$, or $3C$ even in low- Z ions, and they are weak in W^{64+} as well.

Among the dipole-forbidden lines, we have observed the relatively strong $E2L$ line (cf. Fig. 4), which is also relatively prominent in lower- Z neonlike ions. We have not observed the other two $3p \rightarrow 2p$ electric quadrupole transitions, commonly labeled $E2M$ and $E2U$, which have been observed before in mid- Z ions [32, 33, 82]. The $3d_{5/2} \rightarrow 2s_{1/2}$ electric quadrupole line labeled $E2S$, however, was observed and found to be more intense than lines $3A$ and $3B$ (cf. Fig. 7). A measurement of this line in Yb^{60+} , i.e. in the element four atomic numbers lower than tungsten, found this line to be weaker than $3A$ [37]. This trend arises from the

fact that transition rates of forbidden lines increase more strongly as a function of Z than those of dipole-allowed lines.

The energies of the observed neonlike transitions are listed in Table I together with the estimated uncertainty. The measurement uncertainty is comprised of the calibration uncertainty, the accuracy with which the line centroid can be determined, and the uncertainty introduced by spectral drifts (i.e., the reproducibility for the different spectra in which a given line was observed). The energy uncertainty of the strongest lines is ± 0.40 or ± 0.50 eV, as these spectra could be measured relatively quickly and thus several times with different spectrometer settings. The highest uncertainties are associated with the energies of lines $3A$ and $E2S$. Line $3A$ is weak and line $E2S$ falls outside the spectral area spanned by the reference lines from vanadium (cf. Fig. 7).

B. W LXIV spectral lines

The strongest collisional satellite lines from sodiumlike tungsten occur at the low-energy side of the two neonlike lines $3C$ and $3D$. We, thus, expect to observe those lines in Figs. 5 and 7. These transitions are basically all of the type $3d \rightarrow 2p$, and they are all electric dipole transitions. Forbidden transitions cannot effectively compete with the corresponding Auger transition, as all innershell excited sodiumlike levels are autoionizing.

Our identification of the sodiumlike tungsten lines is based on our calculations using FAC together with the transition energies provide by the MBPT calculations by Safronova et al. [42]. These calculations predict five strong transitions in W^{63+} with an intensity above 0.4 photons per ion per second at an electron density of 10^{12} cm^{-3} and an electron beam energy of 16 keV. We have labeled these lines $Na-1$ through $Na-5$ in Fig. 2(a) and have listed them in Table II.

The strongest two W^{63+} lines, labeled $Na-1$ and $Na-2$ are readily identified next to line $3D$ in Fig. 5. Their energies could be determined with an uncertainty of ± 0.50 and ± 0.70

eV, respectively, as given in Table II. The other three lines are weak, as seen from Fig. 7, and their identifications are less certain. The lines, however, have been reproducibly seen in different measurements. Line *Na-3* may be blended with the magnesiumlike tungsten line *Mg-2*. The uncertainty of the transition energy of this possible blended feature is ± 1.0 eV. Line *Na-3*, which starts from upper level $(2p_{1/2}^5 3p_{1/2} 3p_{3/2})_{J=3/2}$, only exists because of interaction with the level $(2p_{3/2}^5 3s_{1/2} 3d_{3/2})_{J=3/2}$.

C. W LXIII spectral lines

We were able to firmly identify only the strongest of the predicted lines in magnesiumlike W^{62+} shown in Fig. 2(b). This line is labeled *Mg-1* and located on the low-energy side of the line *3D*, as shown in Fig. 5. The energy of this line could be measured with an uncertainty of ± 0.6 eV. The second strongest predicted line, which is labeled *Mg-2*, is located near line *3C* (cf. Fig. 7). Its identification is uncertain, as it may blend with line *Na-3* in W^{63+} , as mentioned in the previous section. No other magnesiumlike tungsten transitions could be firmly identified.

A summary of the measured and calculated transitions energies of the two magnesiumlike tungsten lines is given in Table III.

D. W LXII spectral lines

The electron beam energy was chosen to maximize the abundance of W^{64+} ions in the trap. Consequently, the abundance of sodiumlike and magnesiumlike tungsten was expectedly low, and the abundance of aluminumlike W^{61+} ions is expected to be even lower. The strongest W^{61+} lines is predicted to be at 9010.9 eV, as shown in Fig. 2(c). This is close to a weak feature at 9013.2 ± 1.2 eV in the spectral range shown in Fig. 5. However, we are not able to ascertain that this is indeed an aluminumlike tungsten transition. There are no possible features near the predicted location of the second strongest aluminumlike line predicted by

our FAC calculations.

E. W LXVI spectral lines

As part of our process to identify the neonlike tungsten lines and to distinguish them from lines in lower or higher charge states, we have also recorded spectra at beam energies well above the ionization potential of W^{64+} at 15.60 keV [83]. Spectra recorded at 17 and 21 keV show clear evidence of fluorinelike W^{65+} lines, as illustrated by Figs. 4(b), 5(a) and 7(a). As we have done above, we have used our calculations for the W LXVI spectral lines, which are shown in Fig. 3(a), to identify these lines.

Several observed features, i.e. those labeled $F-1$, $F-2$, $F-3$, and $F-6$, are each formed by a single transition. The other features, i.e. $F-4$, $F-5$, and $F-7$, are a blend of two or more transitions that our measurements cannot resolve. In addition, feature $F-4$ is likely a blend with the oxygenlike tungsten line $O-1$.

A summary of our identifications and measured wavelengths of the fluorinelike tungsten lines, including the measurement uncertainties, is given in Table IV.

F. W LXVII spectral lines

All lines associated with a photon production rate higher than 0.2 photons/ion/second predicted by our calculations (cf. Fig. 3(b)) are listed in Table VI. As discussed below, we have firmly identified five out of the eleven lines listed. A sixth line, which we labeled $O-1$, is blended with two fluorinelike tungsten lines and, thus, its identity is uncertain.

We were able to identify lines $O-2$, $O-3$, $O-4$, and $O-5$ in the low-energy region of our spectral measurements, which is shown in Fig. 4(b). Surprisingly, we did not observe line $O-0$ near 8400 eV, although it is predicted to have about the same strength as the lines we did observe.

The strongest of the L-shell W^{66+} lines according to our predictions is line $O-7$. It is seen

only weakly in the spectra in Fig. 5(a) and Fig. 6(a). The fact that it is so weak indicates that the charge balance shifted more toward lower charge states of tungsten during these measurements than during the measurements of the spectral region shown in Fig. 4. Because *O-7* is repeatedly seen in multiple spectra, we are confident about its identity. The adjacent line *O-6*, however, which is predicted to be three times weaker than *O-7*, could not be identified.

The remaining three W^{66+} transitions predicted by our calculations and listed in Table VI are situated at the highest spectral energies, shown in Fig. 7. None of these lines could be identified. Although this spectral region has several unidentified features, none have a wavelength close to those predicted for the strongest oxygenlike lines in this region.

An overview of our identifications and measured transition energies are given in Table V.

V. COMPARISON WITH THEORY

Neonlike ions have received a lot of theoretical attention, however, only few predictions exist for the transition energies of neonlike tungsten. In Table I, we compare our measurements to the calculations of Ivanova and Gulov [49], who used relativistic perturbation theory with a model potential to calculate their values. We also compare to the recent calculations of Vilkas, López-Encarnación, and Ishikawa [39], who used the multireference many-body Møller-Plesset perturbation theory in their work. In addition, we also list our own calculations using FAC.

The energy values from Ivanova and Gulov are consistently higher than our measurements. The differences vary between about 2.7 and 15.5 eV. By contrast, the predictions from FAC are consistently lower than our measured values. The differences vary between 0.4 and 6.0 eV. The energy values from Vilkas et al. are also consistently lower than our measurements. However, overall their values agree best with our measurements, and the differences vary from perfect agreement to 1.3 eV.

The differences between the three calculations and our measurements are illustrated graphically in Fig. 8. This figure shows that the recent calculations using the multireference many-body Møller-Plesset perturbation theory produce results that are almost indistinguishable from the measured results. The differences are at most roughly twice the experimental uncertainties. FAC produces good agreement only for the three lines with the highest energy. The upper levels of these three lines all have a $2s$ vacancy. All other lines, which emanate from upper levels with a $2p$ vacancy, differ substantially from our measurements, i.e., the difference is about ten times the experimental uncertainty. There are no obvious systematic trends in the calculations from Ivanova and Gulov, and good agreement with our measurements is found for none of their energies.

To our knowledge, there are no transition energy (or intensity) predictions in the literature for the collisional satellite lines from oxygenlike and fluorinelike tungsten. As a result, we compare our measurements only to the predictions from FAC (cf. Tables V and VI). We find that the differences are similar in magnitude as those for the neonlike transition energies. Again, the FAC numbers are generally lower in energy. There is only one exception: For one component of feature $F-7$, the FAC value is larger than the measurement. Based on the theoretical predictions, we assume that $F-7$ is a blend of three lines. But it may well be that this component is not part of the blend and otherwise too weak to observe separately.

Our FAC calculations also produce transition energies which are smaller than the measured values for sodiumlike and magnesiumlike tungsten, as the comparison on Tables II and III shows. The differences are between about 1.7 to 4.1 eV. The only exception occurs for the magnesiumlike tungsten line labeled $Mg-2$. In this case, the FAC value is larger than measured, which may reflect the fact that the observed feature is dominated by the sodiumlike tungsten line $Na-3$.

In the case of our sodiumlike tungsten measurements, we can also compare our results with those recently obtained by Safronova et al. [42] using the relativistic many-body perturbation theory. The comparison with the values obtained with this method is given in

Table II. The relativistic many-body perturbation theory method is similar to the relativistic multi-reference Møller-Plesset approach in the sense that it applies perturbation theory to account for electron correlations before diagonalization, while the multi-reference Møller-Plesset approach applies perturbation after diagonalization. We thus expect that the many-body perturbation theory calculations are very accurate. Indeed, the values obtained with this method agree better with our measurements than those produced by our FAC calculations. In addition, two of the calculated values agree with the measured values within the measurement uncertainty, while the remaining three are within two or three times the measurement uncertainties.

VI. CONCLUSIONS

We have provided benchmark atomic data for L-shell tungsten x-ray lines, which have experimental uncertainties that are three to ten times lower than similar data from other neonlike ions with comparably high atomic number. Our data, thus, afford a test of modern atomic theories at high Z . In particular, our measurements of the neonlike W^{64+} spectral lines show that the relativistic multi-reference Møller-Plesset approach [39] provides highly accurate transition energies. The differences are within about twice the experimental uncertainties. Other approaches have discrepancies with the experimental values that are about ten times the experimental uncertainties or more. In addition, we were able to provide benchmark data to test the results obtained with the relativistic many-body perturbation theory for sodiumlike W^{63+} [42]. Again, the calculational approach was validated, as very good agreement between the experimental data and the calculations was found. The maximum difference in this case was about three times the experimental uncertainties.

We note that our measurements provide accurate rest wavelengths that can be used in future measurements of the core plasma motion proposed on the ITER tokamak. Moreover, our identification of collisional satellite lines next to the strongest neonlike tungsten line

at 9126.25 ± 0.50 eV provides an *in situ* means for establishing the spectral dispersion of such future measurements. In particular, we identified two sodiumlike tungsten lines at 9096.0 ± 0.7 and 9088.8 ± 0.5 eV, one magnesiumlike tungsten line at 9055.3 ± 0.6 eV, and one fluorinelike tungsten line at 9256.3 ± 0.6 eV in the vicinity of the neonlike tungsten line $3D$. Finally, we note that all of the collisional satellite lines we have measured are far enough separated from the neonlike line that they will not blend with this line even when the lines are broadened by the extreme thermal motion associated with ITER plasmas. In particular, the Doppler motion in a plasma with a 30 keV ion temperature will broaden the tungsten lines by about 9 eV, while the nearest neighbor is about 30 eV from the neonlike tungsten line. The fact that a line remains well isolated even at high temperature is an important criterion when choosing a spectral line for ion temperature and rotation measurements, and our measurements show that the neonlike tungsten line satisfies this criterion.

Acknowledgments

This work was performed under the auspices of the US DOE by LLNL under contract DE-AC52-07NA-27344 and supported by the Office of Fusion Energy Basic and Applied Plasma Science Initiative and the LLNL Laboratory Direct Research and Development program under project 09-ERD-016. It was carried out as part of the IAEA Coordinated Research Project “Spectroscopic and Collisional Data for Tungsten from 1 eV to 20 keV”. PB and JKL thank Prof. Y. Ishikawa and the University of Puerto Rico for their hospitality during the preparation of this manuscript.

-
- [1] C. R. Canizares, D. P. Huenemoerder, D. S. Davis, D. Dewey, K. A. Flanagan, J. Houck, T. H. Markert, H. L. Marshall, M. L. Schattenburg, N. S. Schulz, M. Wise, J. J. Drake, and N. S. Brickhouse, *Astrophys. J.* **539**, L41 (2000).

- [2] A. C. Brinkman, E. Behar, M. Güdel, M. Audard, A. J. F. den Boggende, G. Branduardi-Raymont, J. Cottam, C. Erd, J. W. den Herder, F. Jansen, J. S. Kaastra, S. M. Kahn, R. Mewe, F. B. S. Paerels, J. R. Peterson, A. P. Rasmussen, I. Sakelliou, and C. de Vries, *Astron. Astrophys.* **365**, L324 (2001).
- [3] A. J. J. Raassen, R. Mewe, M. Audard, M. Güdel, E. Behar, J. S. Kaastra, R. L. J. van der Meer, C. R. Foley, and J.-U. Ness, *Astron. Astrophys.* **389**, 228 (2002).
- [4] H. Xu, S. M. Kahn, J. R. Peterson, E. Behar, F. B. S. Paerels, R. F. Mushotzky, J. G. Jernigan, and K. Makishima, *Astrophys. J.* **579**, 600 (2002).
- [5] J. R. Peterson and A. C. Fabian, *Phys. Rep.* **427**, 1 (2006).
- [6] J. S. Sanders, A. C. Fabian, K. A. Frank, J. R. Peterson, and H. R. Russell, *Mon. Not. R. Astron. Soc.* **402**, 127 (2010).
- [7] M. Ono, P. Beiersdorfer, R. Bell, S. Bernabei, A. Cavallo, A. Chmyga, S. Cohen, P. Colestock, G. Gammel, G. J. Greene, J. Hosea, R. Kaita, I. Lehrman, G. Mazzitelli, E. Mazzucato, D. McNeill, K. Sato, J. Stevens, J. Timberlake, J. R. Wilson, and A. Wouters, *Phys. Rev. Lett.* **60**, 294 (1988).
- [8] P. Beiersdorfer, S. von Goeler, M. Bitter, K. W. Hill, R. A. Hulse, R. S. Walling, *Rev. Sci. Instrum.* **60**, 895 (1989).
- [9] J. E. Rice, E. S. Marmor, F. Bombarda, and L. Qu, *Nucl. Fus.* **37**, 421 (1997).
- [10] B. K. F. Young, A. L. Osterheld, R. S. Walling, W. H. Goldstein, T. W. Phillips, R. E. Stewart, G. Charatis, and Gar. E. Busch, *Phys. Rev. Lett.* **62**, 1266 (1989).
- [11] C. J. Keane, B. A. Hammel, A. L. Osterheld, and D. R. Kania, *Phys. Rev. Lett.* **72**, 3029 (1994).
- [12] M. D. Rosen, P. L. Hagelstein, D. L. Matthews, E. M. Campbell, A. U. Hazi, B. L. Whitten, B. MacGowan, R. E. Turner, R. W. Lee, G. Charatis, Gar. E. Busch, C. L. Shepard, and P. D. Rockett, *Phys. Rev. Lett.* **54**, 106 (1985).
- [13] D. J. Fields, R. S. Walling, G. M. Shimkaveg, B. J. MacGowan, L. B. Da Silva, J. H. Scofield,

- A. L. Osterheld, T. W. Phillips, M. D. Rosen, D. L. Matthews, W. H. Goldstein, and R. E. Stewart, *Phys. Rev. A* **46**, 1606 (1992).
- [14] A. Kramida, *Can. J. Phys.* **89**, 551 (2011).
- [15] C. H. Skinner, *Can. J. Phys.* **86**, 285 (2008).
- [16] A. S. Safronova, V. L. Kantsyrev, P. Neill, U. I. Safronova, D. A. Fedin, N. D. Ouart, M. F. Yilmaz, G. Osborne, I. Shrestha, K. Williamson, T. Hoppe, C. Harris, P. Beiersdorfer, and S. Hansen, *Can. J. Phys.* **86**, 267 (2008).
- [17] Y. Podpaly, J. Clementson, P. Beiersdorfer, J. Williamson, G. V. Brown, and M. F. Gu, *Phys. Rev. A* **80**, 052504 (2009).
- [18] Y. Ralchenko, I. N. Draganic, J. N. Tan, J. D. Gillaspay, J. M. Pomeroy, J. Reader, U. Feldman, and G. E. Holland, *J. Phys. B* **41**, 021003 (2008).
- [19] J. Clementson and P. Beiersdorfer, *Phys. Rev. A* **81**, 052509 (2010).
- [20] T. Pütterich, R. Neu, R. Dux, A. D. Whiteford, M. G. O Mullane, and the ASDEX Upgrade Team, *Plasma Phys. Control. Fusion* **50**, 085016 (2008).
- [21] J. Clementson and P. Beiersdorfer, *Phys. Rev. A* **81**, 052509 (2010).
- [22] J. Clementson, P. Beiersdorfer, G. V. Brown, and M. F. Gu, *Phys. Scripta* **81**, 015301 (2010).
- [23] G. C. Osborne, A. S. Safronova, V. L. Kantsyrev, U. I. Safronova, P. Beiersdorfer, K. Williamson, M. E. Weller, and I. Shrestha, *Can. J. Phys.* **89**, 599 (2011).
- [24] Y. Ralchenko, I. N. Draganić, D. Osin, J. D. Gillaspay, and J. Reader, *Phys. Rev. A* **83**, 032517 (2011).
- [25] C. S. Harte, C. Suzuki, T. Kato, H. A. Sakaue, D. Kato, K. Sato, N. Tamura, S. Sudo, R. D’Arcy, E. Sokell, J. White, and G. O’Sullivan, *J. Phys. B* **43**, 205004 (2010).
- [26] S. Wu and R. Hutton, *Can. J. Phys.* **86**, 125 (2008).
- [27] J. Clementson, P. Beiersdorfer, E. W. Magee, H. S. McLean, and R. D. Wood, *J. Phys. B* **43**, 144009 (2010).
- [28] P. Beiersdorfer, J. Clementson, J. Dunn, M. F. Gu, K. Morris, Y. Podpaly, E. Wang, M.

- Bitter, R. Feder, K. W. Hill, D. Johnson, and R. Barnsley, *J. Phys. B* **43**, 144008 (2010).
- [29] R. Barnsley, M. G. O Mullane, L. C. Ingesson, and A. Malquias, *Rev. Sci. Instrum.* **75**, 3743 (2004).
- [30] P. Beiersdorfer, G. V. Brown, J. Clementson, J. Dunn, K. Morris, E. Wang, R. L. Kelley, C. A. Kilbourne, F. S. Porter, M. Bitter, R. Feder, K. W. Hill, D. Johnson, and R. Barnsley, *Rev. Sci. Instrum.* **81**, 10E323 (2010).
- [31] C. Biedermann, R. Radtke, R. Seidel, and T. Pütterich, *Phys. Scripta* **T134**, 014026 (2009).
- [32] P. Beiersdorfer, M. Bitter, S. von Goeler, S. Cohen, K. W. Hill, J. Timberlake, R. S. Walling, M. H. Chen, P. L. Hagelstein, and J. H. Scofield, *Phys. Rev. A* **34**, 1297 (1986).
- [33] P. Beiersdorfer, S. von Goeler, M. Bitter, E. Hinnov, R. Bell, S. Bernabei, J. Felt, K. W. Hill, R. Hulse, J. Stevens, S. Suckewer, J. Timberlake, A. Wouters, M. H. Chen, J. H. Scofield, D. D. Dietrich, M. Gerassimenko, E. Silver, R. S. Walling, and P. L. Hagelstein, *Phys. Rev. A* **37**, 4153 (1988).
- [34] P. Beiersdorfer, Ph.D. thesis, Princeton University (1988).
- [35] G. A. Chandler, M. H. Chen, D. D. Dietrich, P. O. Egan, K. P. Ziock, P. H. Mokler, S. Reusch, and D. H. H. Hoffmann, *Phys. Rev. A* **39**, 565 (1989).
- [36] D. D. Dietrich, A. Simionovici, M. H. Chen, G. Chandler, C. J. Hailey, P. O. Egan, P. H. Mokler, S. Reusch, and D. H. H. Hoffmann, *Phys. Rev. A* **41**, 1450 (1990).
- [37] P. Beiersdorfer, M. H. Chen, R. E. Marrs, and M. A. Levine, *Phys. Rev. A* **41**, 3453 (1990).
- [38] P. Beiersdorfer, *Nucl. Instrum. Methods* **B56/57**, 1144 (1991).
- [39] M. J. Vilkas, J. M. López-Encarnación, and Y. Ishikawa, *At. Data Nucl. Data Tables* **94**, 50 (2008).
- [40] Y. Ishikawa, J. M. López Encarnación, and E. Träbert, *Phys. Scripta* **79**, 025301 (2009).
- [41] P. Beiersdorfer, F. Diaz, and Y. Ishikawa, *Astrophys. J.* **745**, 167 (2012).
- [42] U. I. Safronova, A. S. Safronova, and P. Beiersdorfer, *At. Data Nucl. Data Tables* **95**, 751 (2009).

- [43] M. Klapisch, *Comput. Phys. Commun.* **2**, 239 (1971).
- [44] U. I. Safronova and J.-F. Wyart, *Phys. Scripta* **46**, 134 (1992).
- [45] F. A. Parpia, C. F. Fischer, and I. P. Grant, *Comp. Phys. Comm.* **94**, 249 (1996).
- [46] E. Avgoustoglou, W. R. Johnson, D. R. Plante, J. Sapirstein, S. Sheinerman, and S. A. Blundell, *Phys. Rev. A* **46**, 5478 (1992).
- [47] E. Avgoustoglou, W. R. Johnson, Z. W. Liu, and J. Sapirstein, *Phys. Rev. A* **51**, 1196 (1995).
- [48] U. I. Safronova, C. Namba, I. Murakami, W. R. Johnson, and M. S. Safronova, *Phys. Rev. A* **64**, 012507 (2001).
- [49] E. P. Ivanova and A. V. Gulov, *At. Data Nucl. Data Tables* **49**, 1 (1991).
- [50] M. F. Gu, *Can. J. Phys.* **86**, 675 (2008).
- [51] P. Beiersdorfer, M. Obst, and U. I. Safronova, *Phys. Rev. A* **83**, 012514 (2011).
- [52] P. Beiersdorfer, T. W. Phillips, K. L. Wong, R. E. Marrs, and D. A. Vogel, *Phys. Rev. A* **46**, 3812 (1992).
- [53] M. F. Gu, P. Beiersdorfer, and J. K. Lepson, *Astrophys. J.* **732**, 91 (2011).
- [54] H. Chen, M. F. Gu, E. Behar, G. V. Brown, S. M. Kahn, and P. Beiersdorfer, *Astrophys. J. (Suppl.)* **168**, 319 (2007).
- [55] M. F. Gu, P. Beiersdorfer, G. V. Brown, H. Chen, D. B. Thorn, and S. M. Kahn, *Astrophys. J.* **657**, 1172 (2007).
- [56] P. Beiersdorfer, *Can. J. Phys.* **86**, 1 (2008).
- [57] R. E. Marrs, *Can. J. Phys.* **86**, 11 (2008).
- [58] S. Chantrenne, P. Beiersdorfer, R. Cauble, and M. B. Schneider, *Phys. Rev. Lett.* **69**, 265 (1992).
- [59] K. L. Wong, P. Beiersdorfer, K. J. Reed, and D. A. Vogel, *Phys. Rev. A* **51**, 1214 (1995).
- [60] K. Widmann, P. Beiersdorfer, V. Decaux, and M. Bitter, *Phys. Rev. A* **53**, 2200 (1996).
- [61] V. Decaux, P. Beiersdorfer, S. M. Kahn, and V. L. Jacobs, *Astrophys. J.* **482**, 1076 (1997).
- [62] P. Beiersdorfer, M. Bitter, D. Hey, and K. J. Reed, *Phys. Rev. A* **66**, 032504 (2002).

- [63] P. Beiersdorfer, R. E. Marrs, J. R. Henderson, D. A. Knapp, M. A. Levine, D. B. Platt, M. B. Schneider, D. A. Vogel, and K. L. Wong, *Rev. Sci. Instrum.* **61**, 2338 (1990).
- [64] A. Burek, *Space Sci. Instrum.* **2**, 53 (1976).
- [65] D. Vogel, P. Beiersdorfer, V. Decaux, and K. Widmann, *Rev. Sci. Instrum.* **66**, 776 (1995).
- [66] J. H. Parkinson, *Astron. Astrophys.* **24**, 215 (1973).
- [67] A. H. Gabriel, *Mon. Not. R. Astron. Soc.* **160**, 99 (1972).
- [68] P. Beiersdorfer, M. Bitter, S. von Goeler, and K. W. Hill, *Phys. Rev. A* **40**, 150 (1989).
- [69] C. T. Chantler, D. Paterson, L. T. Hudson, F. G. Serpa, J. D. Gillaspy, and E. Takács, *Phys. Rev. A* **62**, 042501 (2000).
- [70] P. Beiersdorfer, *Can. J. Phys.* **87**, 9 (2009).
- [71] J. D. Gillaspy, T. Lin, L. Tedesco, J. N. Tan, J. M. Pomeroy, J. M. Laming, N. Brickhouse, G. Chen, and E. Silver, *Astrophys. J.* **728**, 132 (2011).
- [72] W. R. Johnson and G. Soff, *At. Data Nucl. Data Tables* **33**, 405 (1985).
- [73] G. W. F. Drake, *Can. J. Phys.* **66**, 586 (1988).
- [74] I. G. Brown, J. E. Galvin, R. A. MacGill, and R. T. Wright, *Appl. Phys. Lett.* **49**, 1019 (1986).
- [75] P. Beiersdorfer, A. L. Osterheld, M. H. Chen, J. R. Henderson, D. A. Knapp, M. A. Levine, R. E. Marrs, K. J. Reed, M. B. Schneider, and D. A. Vogel, *Phys. Rev. Lett.* **65**, 1995 (1990).
- [76] A. H. Compton and S. K. Allison, *X-Rays in Theory and Experiment*, 2nd ed. (D. van Nostrand, Princeton, 1935).
- [77] P. Beiersdorfer, V. Decaux, S. Elliott, K. Widmann, and K. Wong, *Rev. Sci. Instrum.* **66**, 303 (1995).
- [78] P. Beiersdorfer, V. Decaux, and K. Widmann, *Nucl. Instrum. Methods* **B98**, 566 (1995).
- [79] P. Beiersdorfer, A. L. Osterheld, V. Decaux, and K. Widmann, *Phys. Rev. Lett.* **77**, 5353 (1996).
- [80] P. Beiersdorfer, J. R. Crespo-López Urrutia, E. Förster, J. Mahiri, and K. Widmann, *Rev. Sci. Instrum.* **68**, 1077 (1997).

- [81] N. Nakamura, D. Kato, and S. Ohtani, *Phys. Rev. A* **61**, 052510 (2000).
- [82] D. D. Dietrich, G. A. Chandler, R. J. Fortner, C. J. Hailey, and R. E. Stewart, *Phys. Rev. Lett.* **54**, 1008 (1985).
- [83] P. Beiersdorfer, M. J. May, J. H. Scofield, and S. B. Hansen, *High Energy Dens. Phys.* **8**, 271 (2012).

TABLE I: Comparison of measured and calculated energies of transitions in neonlike W^{64+} . E_{FAC} has been calculated in the present work using the Flexible Atomic Code; E_{Vilkas} are values from [39]; $E_{Ivanova}$ are values from [49]. ΔE is the difference between the mean measured and the calculated values. All transitions decay from the given upper level to the $(1s^2 2s^2 2p^6)_{J=0}$ ground level.

| Label | Upper Level | $E_{Measured}$ (eV) | E_{FAC} | ΔE_{FAC} | E_{Vilkas} | ΔE_{Vilkas} | $E_{Ivanova}$ | $\Delta E_{Ivanova}$ |
|-------|------------------------------------|---------------------|-----------|------------------|--------------|---------------------|---------------|----------------------|
| M2 | $(2s^2 2p_{3/2}^5 3s_{1/2})_{J=2}$ | 8299.22 ± 0.40 | 8293.53 | +5.69 | 8298.33 | +0.89 | 8303.48 | -4.26 |
| 3G | $(2s^2 2p_{3/2}^5 3s_{1/2})_{J=1}$ | 8307.51 ± 0.40 | 8302.17 | +5.34 | 8306.76 | +0.75 | 8312.05 | -4.54 |
| E2L | $(2s^2 2p_{3/2}^5 3p_{1/2})_{J=2}$ | 8450.14 ± 0.60 | 8444.29 | +5.85 | 8448.81 | +1.33 | 8452.82 | -2.68 |
| 3E | $(2s^2 2p_{3/2}^5 3d_{3/2})_{J=1}$ | 8996.31 ± 0.50 | 8990.27 | +6.04 | 8995.16 | +1.15 | 9003.28 | -6.97 |
| 3D | $(2s^2 2p_{3/2}^5 3d_{5/2})_{J=1}$ | 9126.25 ± 0.50 | 9120.69 | +5.56 | 9125.28 | +0.97 | 9139.40 | -13.15 |
| 3F | $(2s^2 2p_{1/2}^5 3s_{1/2})_{J=1}$ | 9689.29 ± 0.50 | 9683.97 | +5.32 | 9687.95 | +1.34 | 9693.38 | -4.09 |
| 3B | $(2s_{1/2} 2p^6 3p_{1/2})_{J=1}$ | 10317.23 ± 0.50 | 10316.87 | +0.36 | 10317.23 | 0.00 | 10323.16 | -5.93 |
| 3C | $(2s^2 2p_{1/2}^5 3d_{3/2})_{J=1}$ | 10408.69 ± 0.40 | 10404.15 | +4.54 | 10407.41 | +1.28 | 10416.30 | -7.61 |
| 3A | $(2s_{1/2} 2p^6 3p_{3/2})_{J=1}$ | 10706.85 ± 0.90 | 10706.00 | +0.85 | 10705.64 | +1.21 | 10715.91 | -9.06 |
| E2S | $(2s_{3/2} 2p^6 3d_{5/2})_{J=2}$ | 10967.75 ± 1.20 | 10966.64 | +1.11 | 10966.90 | +0.85 | 10983.23 | -15.48 |

TABLE II: Comparison of measured and calculated energies of transitions in sodiumlike W^{63+} . E_{FAC} has been calculated in the present work using the Flexible Atomic Code; E_{MBPT} are values from [42] using many-body perturbation theory. ΔE is the difference between the mean measured and calculated values. The line intensity given in photons/ion/second was calculated with FAC at an electron beam energy of 16 keV and an electron density of $1 \times 10^{12} \text{ cm}^3$.

| Label | Upper Level | Lower Level | $E_{measured}$ | E_{FAC} | ΔE_{FAC} | E_{MBPT} | ΔE_{MBPT} | Intensity |
|-------------------|--|---------------------|-------------------|-----------|------------------|------------|-------------------|-----------|
| Na-1 | $(2p_{3/2}^5 3s_{1/2} 3d_{5/2})_{J=3/2}$ | $(2p^6 3s)_{J=1/2}$ | 9088.8 ± 0.5 | 9086.09 | 2.7 | 9090.32 | -1.5 | 4.9 |
| Na-2 | $(2p_{3/2}^5 3s_{1/2} 3d_{5/2})_{J=1/2}$ | $(2p^6 3s)_{J=1/2}$ | 9096.0 ± 0.7 | 9092.75 | 3.2 | 9095.86 | 0.1 | 2.3 |
| Na-3 ^a | $(2p_{1/2}^5 3p_{1/2} 3p_{3/2})_{J=3/2}$ | $(2p^6 3s)_{J=1/2}$ | 10350.1 ± 1.0 | 10348.41 | 1.7 | 10349.53 | 0.6 | 0.4 |
| Na-4 | $(2p_{1/2}^5 3s_{1/2} 3d_{3/2})_{J=1/2}$ | $(2p^6 3s)_{J=1/2}$ | 10367.3 ± 1.0 | 10463.16 | 4.1 | 10364.76 | 2.6 | 0.7 |
| Na-5 | $(2p_{1/2}^5 3s_{1/2} 3d_{3/2})_{J=3/2}$ | $(2p^6 3s)_{J=1/2}$ | 10381.2 ± 1.0 | 10378.56 | 2.6 | 10378.67 | 2.5 | 0.9 |

^ablended with line $Mg-3$

TABLE III: Comparison of measured and calculated energies of transitions in magnesiumlike W^{62+} . E_{FAC} has been calculated in the present work using the Flexible Atomic Code. ΔE is the difference between the mean measured and calculated values. The line intensity given in photons/ion/second was calculated with FAC at an electron beam energy of 16 keV and an electron density of 1×10^{12} cm^3 .

| Label | Upper Level | Lower level | $E_{measured}$ | E_{FAC} | ΔE_{FAC} | Intensity |
|-------------------|------------------------------------|---------------------|-------------------|-----------|------------------|-----------|
| Mg-1 | $(2p_{3/2}^5 3s^2 3d_{5/2})_{J=1}$ | $(2p^6 3s^2)_{J=0}$ | 9055.3 ± 0.6 | 9053.15 | 2.1 | 6.9 |
| Mg-2 ^a | $(2p_{1/2}^5 3s^2 3d_{3/2})_{J=1}$ | $(2p^6 3s^2)_{J=0}$ | 10350.1 ± 1.2 | 10350.17 | -0.1 | 1.0 |

^ablended with line $\overline{Na-3}$

TABLE IV: Comparison of measured and calculated energies of transitions in fluorinelike W^{65+} . E_{FAC} has been calculated in the present work using the Flexible Atomic Code. ΔE is the difference between the mean measured and calculated values. The line intensity given in photons/ion/second was calculated with FAC at an electron beam energy of 21 keV and an electron density of 1×10^{12} cm^3 .

| Label | Upper Level | Lower Level | $E_{measured}$ | E_{FAC} | ΔE_{FAC} | Intensity |
|------------------|--|------------------------|-------------------|-----------|------------------|-----------|
| F-1 | $(2p_2^4 3s_{1/2})_{J=5/2}$ | $(2p_{3/2}^5)_{J=3/2}$ | 8455.4 ± 0.6 | 8449.78 | 5.6 | 1.0 |
| F-2 | $(2p_2^4 3s_{1/2})_{J=3/2}$ | $(2p_{3/2}^5)_{J=3/2}$ | 8466.0 ± 0.6 | 8460.98 | 5.0 | 1.0 |
| F-3 | $(2p_0^4 3s_{1/2})_{J=1/2}$ | $(2p_{3/2}^5)_{J=3/2}$ | 8519.7 ± 0.6 | 8514.50 | 5.2 | 0.8 |
| F-4 ^a | $(2p_{1/2}^2 2p_{3/2}^3 3p_{1/2})_{J=1/2}$ | $(2p_{1/2}^5)_{J=1/2}$ | 8592.7 ± 0.7 | 8588.59 | 4.1 | 0.40 |
| F-4 ^a | $(2p_2^4 3p_{1/2})_{J=3/2}$ | $(2p_{3/2}^5)_{J=3/2}$ | 8592.7 ± 0.7 | 8586.58 | 6.1 | 0.10 |
| F-5 | $(2p_2^4 3d_{5/2})_{J=5/2}$ | $(2p_{3/2}^5)_{J=3/2}$ | 9256.3 ± 0.6 | 9252.82 | 3.5 | 2.4 |
| F-5 | $(2p_2^4 3d_{5/2})_{J=3/2}$ | $(2p_{3/2}^5)_{J=3/2}$ | 9256.3 ± 0.6 | 9254.10 | 2.2 | 1.9 |
| F-6 | $(2p_0^4 3d_{5/2})_{J=5/2}$ | $(2p_{3/2}^5)_{J=3/2}$ | 9291.5 ± 1.0 | 9289.25 | 2.2 | 1.6 |
| F-7 | $(2p_{1/2} 2p_{3/2}^3 3d_{3/2})_{J=1/2}$ | $(2p_{3/2}^5)_{J=3/2}$ | 10562.2 ± 0.5 | 10557.93 | 4.3 | 0.4 |
| F-7 | $(2p_{1/2} 2p_{3/2}^3 3d_{3/2})_{J=5/2}$ | $(2p_{3/2}^5)_{J=3/2}$ | 10562.2 ± 0.5 | 10559.41 | 2.8 | 1.1 |
| F-7 | $(2p_{1/2} 2p_{3/2}^3 3d_{3/2})_{J=3/2}$ | $(2p_{3/2}^5)_{J=3/2}$ | 10562.2 ± 0.5 | 10564.62 | -2.4 | 0.9 |

^ablended with line $O-1$.

TABLE V: Comparison of measured and calculated energies of transitions in oxygenlike W^{66+} . E_{FAC} has been calculated in the present work using the Flexible Atomic Code. ΔE is the difference between the mean measured and calculated values. The line intensity given in photons/ion/second was calculated with FAC at an electron beam energy of 21 keV and an electron density of 1×10^{12} cm^3 .

| Label | Upper Level | Lower Level | $E_{measured}$ | E_{FAC} | ΔE_{FAC} | Intensity |
|------------------|---|--|------------------|-----------|------------------|-----------|
| O-0 | $(2s^2_2 2p_{1/2} 2p_{3/2}^2 3p_{1/2})_{J=2}$ | $(2s_{1/2} 2p_{1/2}^2 2p_{3/2}^3)_{J=2}$ | | 8400.61 | | 0.3 |
| O-1 ^a | $(2s^2 2p_{1/2}^2 2p_{3/2} 3s_{1/2})_{J=1}$ | $(2s^2 2p_{1/2}^2 2p_{3/2}^2)_{J=0}$ | 8592.7 ± 0.7 | 8588.40 | 4.3 | 0.2 |
| O-2 | $(2s_{1/2} 2p_{1/2}^2 2p_{3/2}^2 3s_{1/2})_{J=2}$ | $(2s_{1/2} 2p_{1/2}^2 2p_{3/2}^3)_{J=2}$ | 8599.4 ± 1.0 | 8595.26 | 3.1 | 0.3 |
| O-3 | $(2s_{1/2} 2p_{1/2}^2 2p_{3/2}^2 3s_{1/2})_{J=2}$ | $(2s_{1/2} 2p_{1/2}^2 2p_{3/2}^3)_{J=1}$ | 8607.1 ± 1.0 | 8604.21 | 2.9 | 0.3 |
| O-4 | $(2s^2 2p_{1/2}^2 2p_{3/2} 3s_{1/2})_{J=2}$ | $(2s^2 2p_{1/2}^2 2p_{3/2}^2)_{J=2}$ | 8644.5 ± 0.6 | 8640.19 | 4.4 | 0.8 |
| O-5 | $(2s^2 2p_{1/2}^2 2p_{3/2} 3s_{1/2})_{J=1}$ | $(2s^2 2p_{1/2}^2 2p_{3/2}^2)_{J=2}$ | 8654.4 ± 0.6 | 8649.51 | 4.9 | 0.4 |
| O-6 | $(2s^2 2p_{1/2}^2 2p_{3/2} 3d_{5/2})_{J=2}$ | $(2s^2 2p_{1/2}^2 2p_{3/2}^2)_{J=2}$ | | 9396.90 | | 0.9 |
| O-7 | $(2s^2 2p_{1/2}^2 2p_{3/2} 3d_{5/2})_{J=3}$ | $(2s^2 2p_{1/2}^2 2p_{3/2}^2)_{J=2}$ | 9413.6 ± 1.2 | 9413.02 | 0.5 | 2.8 |
| O-8 | $(2s^2 2p_{1/2} 2p_{3/2}^2 3d_{3/2})_{J=3}$ | $(2s^2 2p_{1/2}^2 2p_{3/2}^2)_{J=2}$ | | 10712.38 | | 1.1 |
| O-9 | $(2s^2 2p_{1/2} 2p_{3/2}^2 3d_{3/2})_{J=2}$ | $(2s^2 2p_{1/2}^2 2p_{3/2}^2)_{J=2}$ | | 10714.94 | | 0.8 |
| O-10 | $(2s^2 2p_{1/2} 2p_{3/2}^2 3d_{3/2})_{J=1}$ | $(2s^2 2p_{1/2}^2 2p_{3/2}^2)_{J=2}$ | | 10721.66 | | 0.4 |

^ablended with line $F-4$.

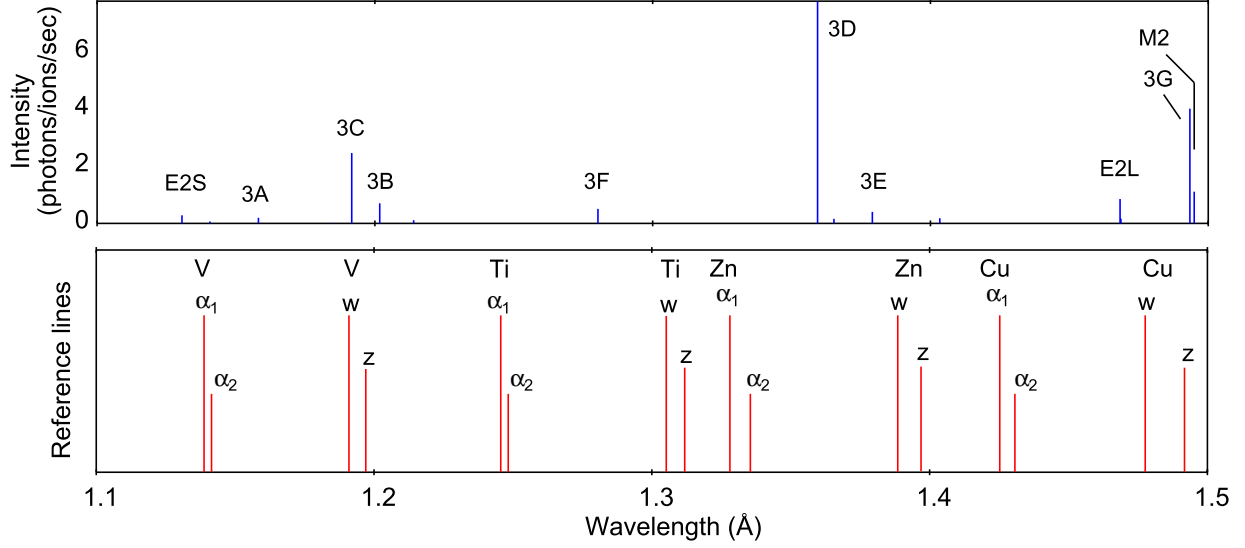


FIG. 1: Top: X-ray spectrum of neonlike W^{64+} calculated with FAC assuming an electron beam energy of 16 keV and an electron density of $1 \times 10^{12} \text{ cm}^{-3}$. The lines are labeled using the notation of Parkinson [66], augmented by the notation of Beiersdorfer et al. [33] for denoting the electric-dipole forbidden lines. Bottom: Schematic location of the reference lines from heliumlike and hydrogenlike ions used for calibration. The heliumlike lines denoted w and z refer to the transitions from levels $1s2p \ ^1P_1$ and $1s2s \ ^3S_1$ to the $1s^2 \ ^1S_0$ ground state, respectively. $\text{Ly-}\alpha_1$ and $\text{Ly-}\alpha_2$ refer to the $2p_{3/2} \rightarrow 1s_{1/2}$ and the $2p_{1/2} \rightarrow 1s_{1/2}$ transitions in the hydrogenlike ions, respectively.

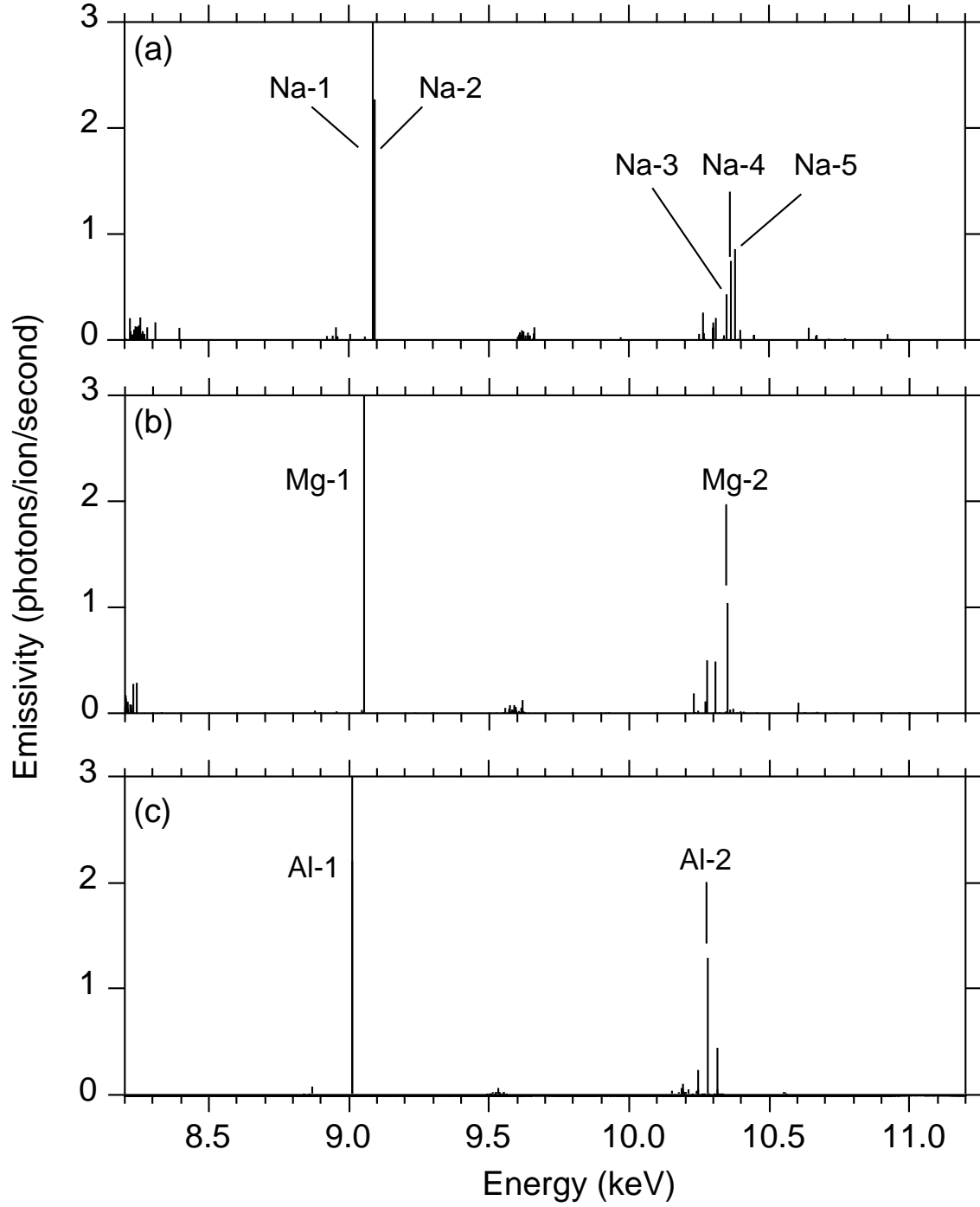


FIG. 2: Spectral emission of (a) sodiumlike W^{63+} , (b) magnesiumlike W^{62+} , and (c) aluminumlike W^{61+} calculated with FAC. The electron energy is assumed to be 16 keV, and the electron density is set to 10^{12} cm^{-3} .

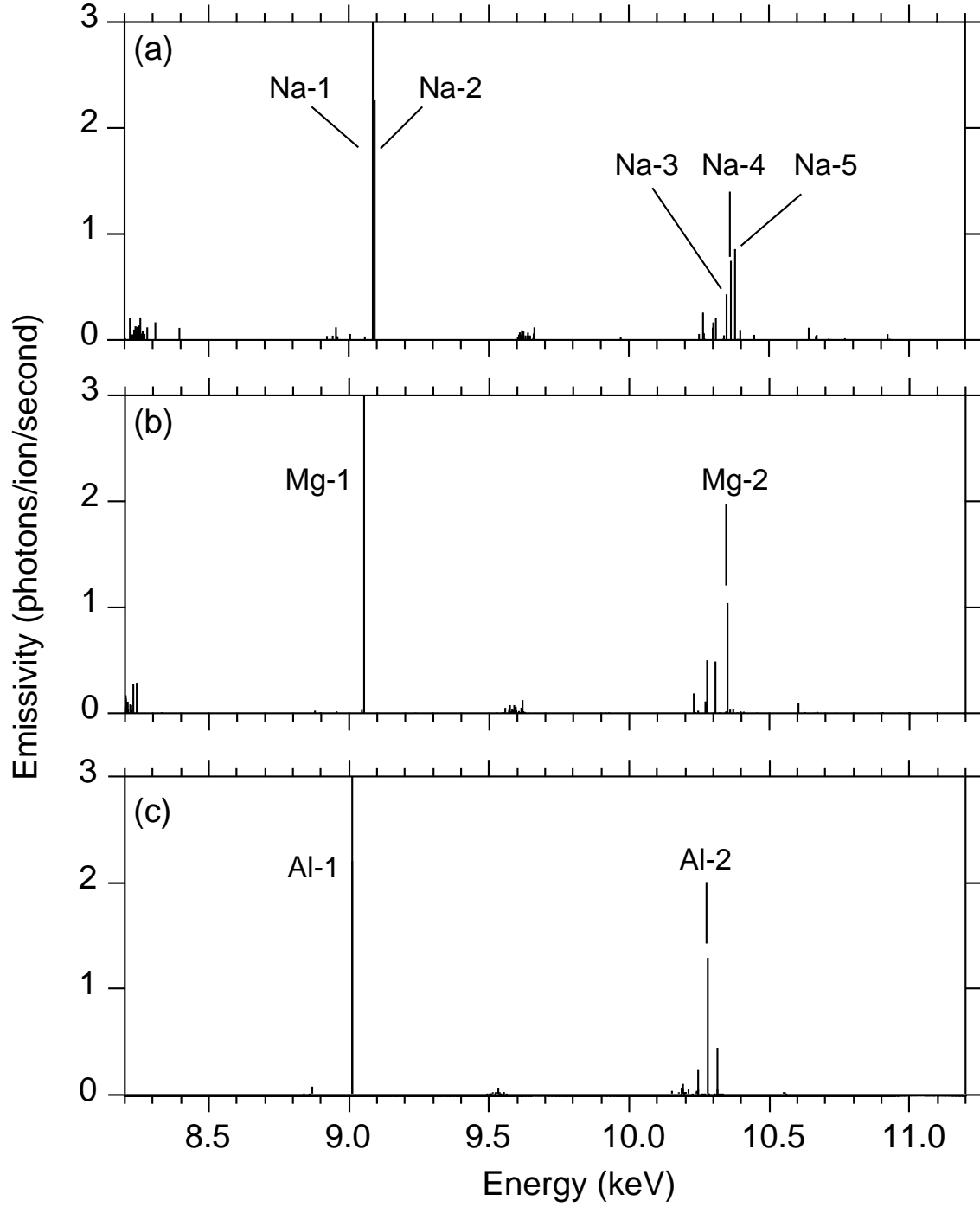


FIG. 3: Spectral emission of (a) fluorinelike W^{65+} and (b) oxygenlike W^{66+} calculated with FAC.

The electron energy is assumed to be 21 keV, and the electron density is set to 10^{12} cm^{-3} .

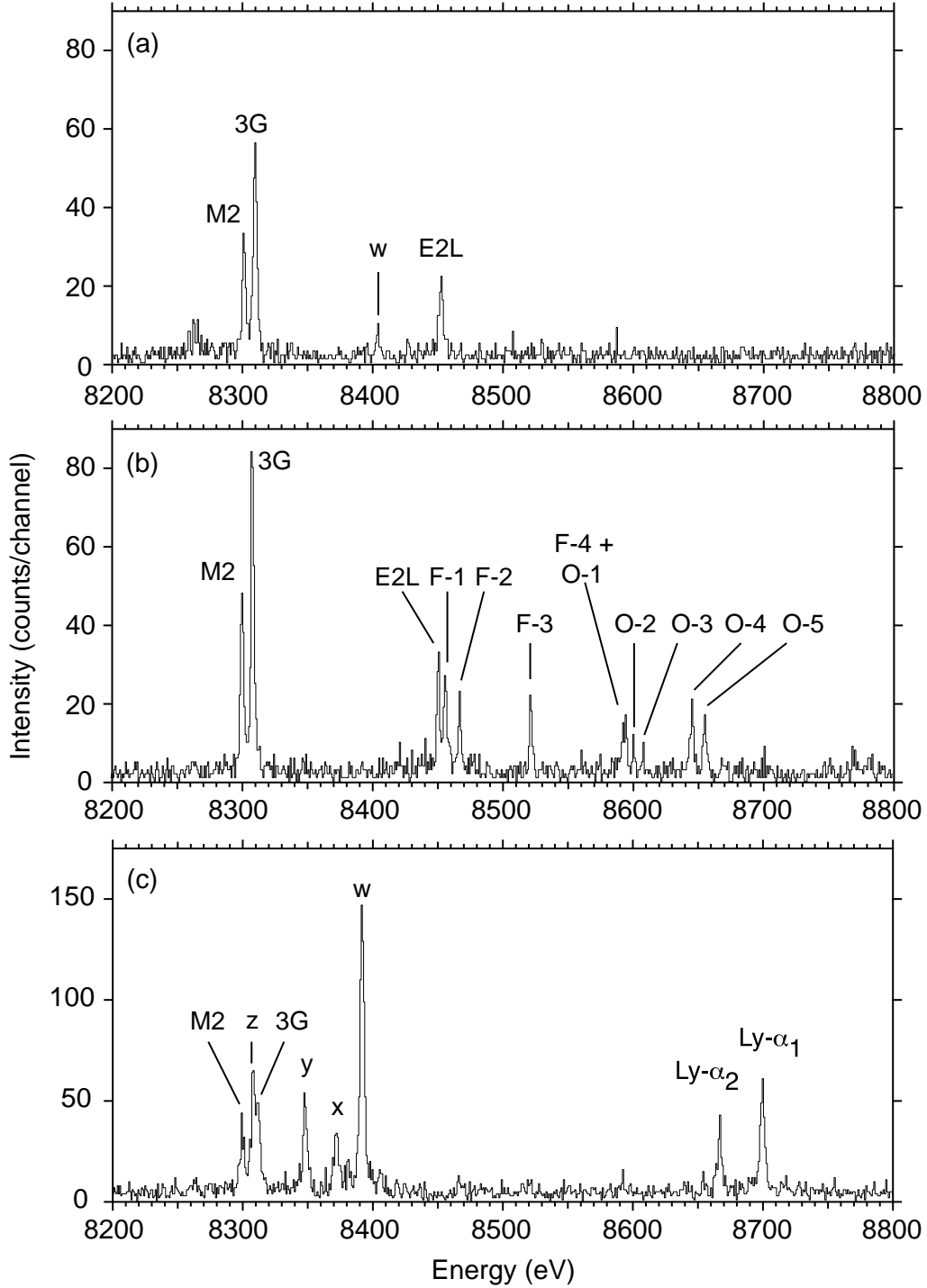


FIG. 4: X-ray emission of neonlike W^{64+} between 8200 and 8800 eV excited at an electron beam energy of (a) 15 keV and (b) 21 keV. The reference spectra of heliumlike and hydrogenlike copper produced at a beam energy of 17.5 keV are shown in (c).

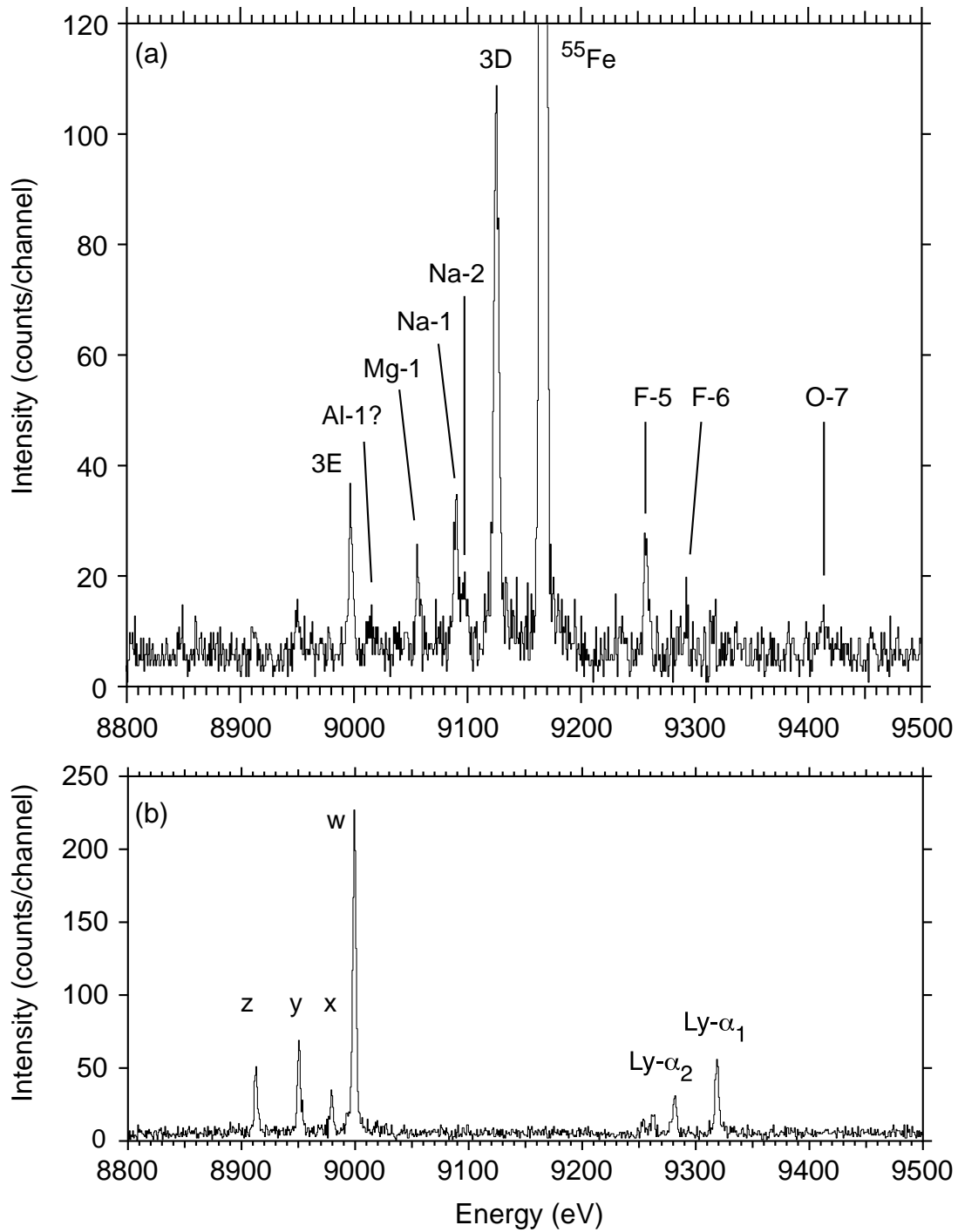


FIG. 5: (a) X-ray emission of neonlike W^{64+} between 8800 and 9500 eV excited at an electron beam energy of 21 keV. The reference spectra of heliumlike and hydrogenlike zinc produced at an electron energy of 17.5 keV are shown in (b).

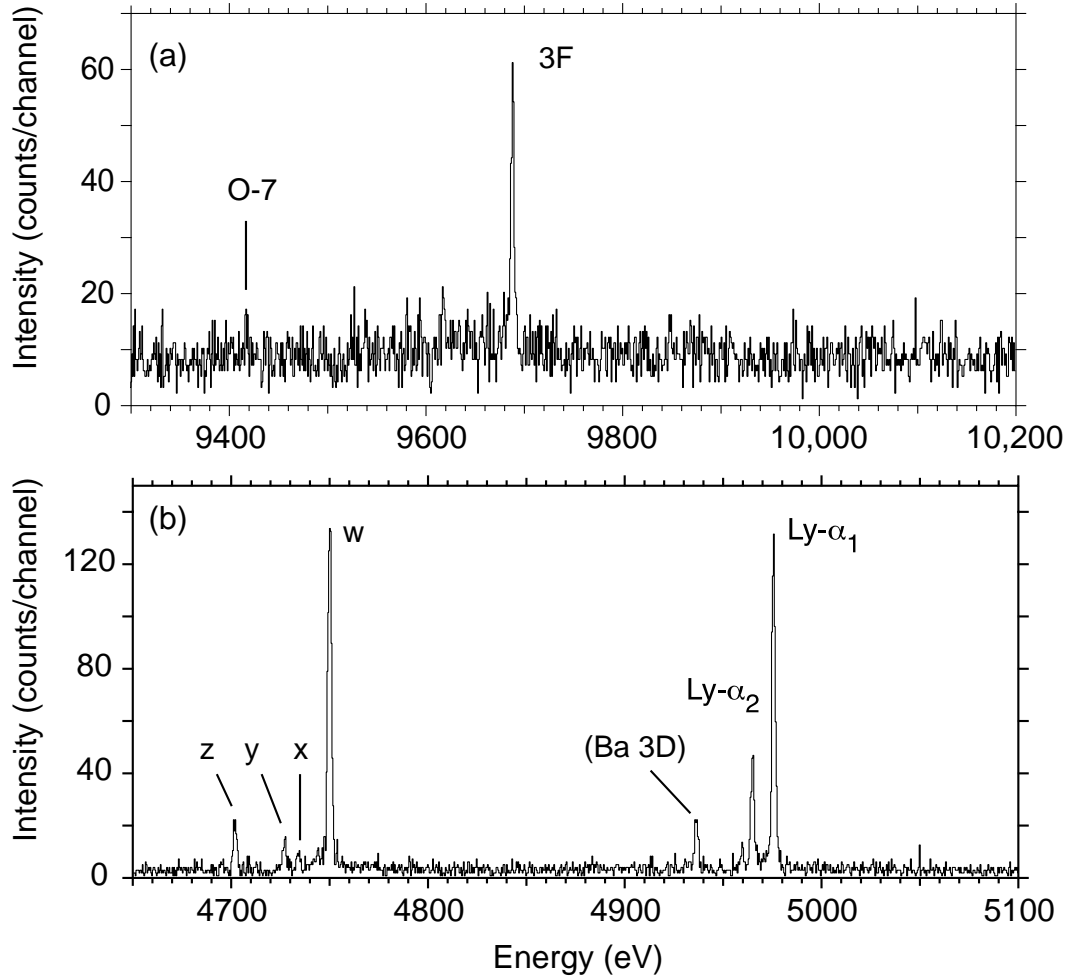


FIG. 6: (a) X-ray emission of neonlike W^{64+} between 9300 and 10,200 eV excited at an electron beam energy of 17 keV. The spectrum was recorded in second order Bragg reflection. The reference spectra of heliumlike and hydrogenlike titanium, which were recorded in first order, are shown in (b).

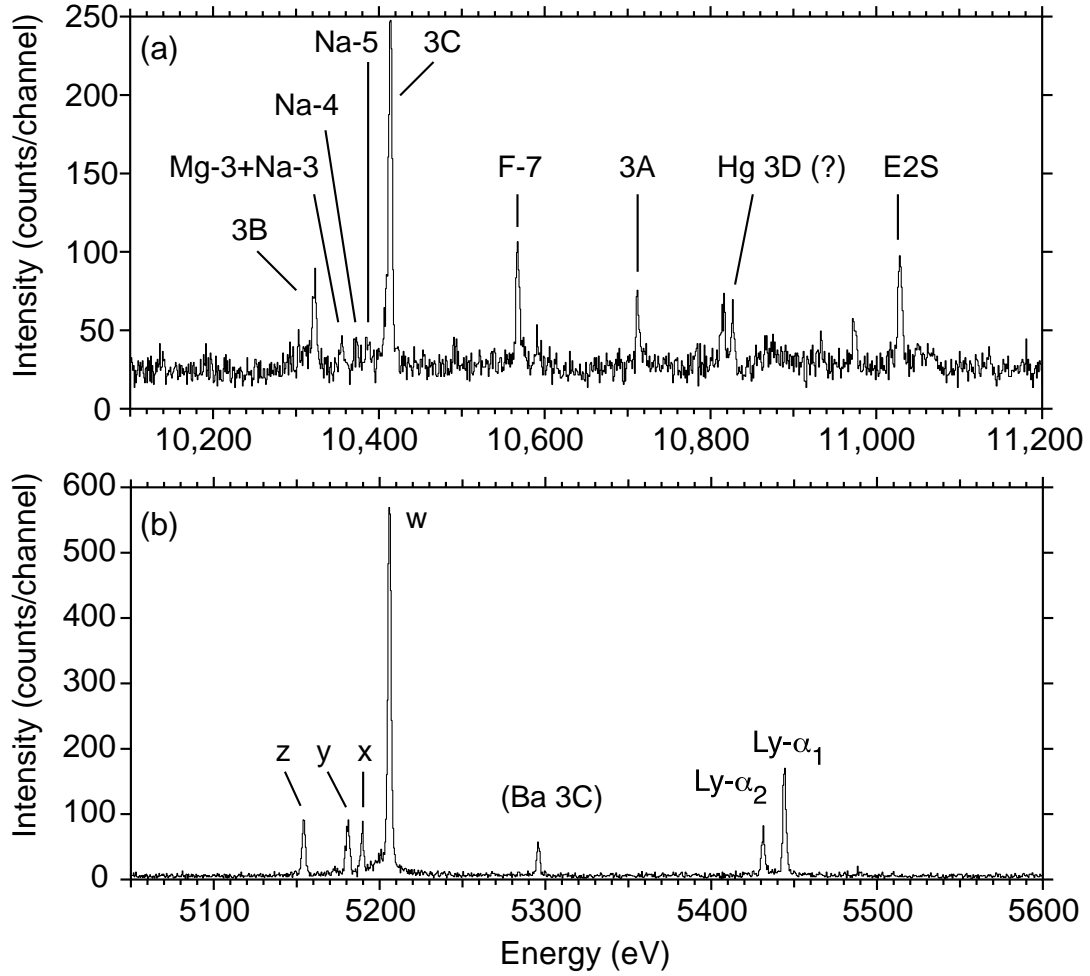


FIG. 7: (a) X-ray emission of neonlike W^{64+} between 10,100 and 11,200 eV excited at an electron beam energy of 17 keV. The spectrum was recorded in second order Bragg reflection. The reference spectra of heliumlike and hydrogenlike vanadium obtained at an electron energy of 7 keV and recorded in first order are shown in (b).

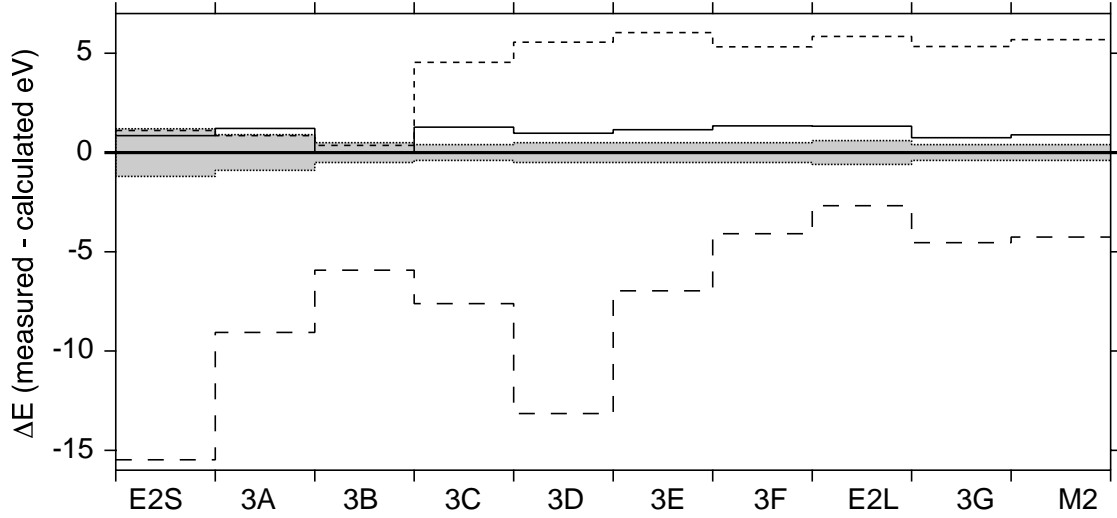


FIG. 8: Comparison between the measured and calculated transition energies of neonlike W^{64+} . The transitions are labeled in the notation used in Table I and are given in order of increasing wavelength. The shaded area indicates the measurement uncertainty. The calculated values are from [49] (long-dashed trace), from [39] (solid trace), and from our own predictions using FAC (short-dashed trace).